ADVANCED MATERIALS
www.advmat.de

Na^+-Complexed Dendritic Polyglycerols for Recovery of Frozen Cells and Their Network in Media

Tae Kyung Won, Aram Shin, Sang Yup Lee, Byeong-Su Kim, and Dong June Ahn**

In this study, a novel phenomenon is identified where precise control of topology and generation of polyglycerol induce the retention of Na^+ ions in biological buffer systems, effectively inhibiting ice crystal growth during cryopreservation. Unlike linear and hyperbranched counterparts, densely-packed hydroxyl and ether groups in 4th-generation dendritic polyglycerol interact with the ions, activating the formation of hydrogen bonding at the ice interface. By inhibiting both intra- and extracellular ice growth and recrystallization, this biocompatible dendritic polyglycerol proves highly effective as a cryoprotectant; hence, achieving the cell recovery rates of ≈134–147%, relative to those of 10% dimethyl sulfoxide, which is a conventional cryoprotectant for human tongue squamous carcinoma (HSC-3) cell line and human umbilical vein endothelial (HUVEC) cells. Further, it successfully recovers the network-forming capabilities of HUVEC cells to ≈89% in tube formation after thawing. The Na^+ ion retention-driven ice-growth inhibition activity in biological media highlights the unique properties of dendritic polyglycerol and introduces a new topological concept for cell-cryoprotectant development.

1. Introduction

Cryopreservation, being vastly involved in coldchain logistics of biological products operating under sub-zero temperatures, is crucial for basic research and various applications in biomedical engineering and clinical practice.[1–5] However, ice crystallization during freezing and thawing can cause significant damage to biological samples. To mitigate this, cryoprotectants (CPAs) such as dimethyl sulfoxide (DMSO)[6] and glycerol[7] are widely used, typically added in large quantities to enable deferred freezing or vitrification. While these low-molecular weight CPAs are effective to a certain degree, they face challenges in preserving complex biological systems such as human embryonic stem cells, cell monolayers, and multicellular systems.[8–10] Current strategies involve developing materials that mimic antifreeze proteins (AFPs) found in nature.[11] It is well-established that AFPs bind to ice through specific amino acid sequences inducing antifreeze activity via the Kelvin effect.[12–14] Subsequent studies have designed various materials, including polymers,[15–18] polypeptides,[19,20] and nanoparticles,[21–27] to inhibit ice crystal growth through strong hydrogen bond formation with the ice crystal face.[28] However, it should be noted that their effectiveness can be diminished in biological media containing high salt concentrations because the design of these materials mainly relies on their binding affinity through hydrogen bonding to the ice interface.[18]

Polyglycerol (PG) features a polyether backbone with hydroxyl groups, offering exceptional structural stability, hydrophilicity, and flexibility, making it ideal for hydrogen bonding with water. Its excellent biocompatibility makes it valuable for applications in biology, cosmetics, pharmaceuticals, and food.[29,30] Linear polyglycerol (*lin*PG), with its flexible structure capable of high internal flexibility compared to hyperbranched polyglycerol (*hb*PG), has proven useful for molecular recognition and interactions with cell surfaces.[31] The distinct branching patterns of polyglycerol significantly influence its properties and applications. Dendritic polyglycerol (*d*PG) features a fully branched architecture with no linear units, corresponding to a degree of branching (DB) of 1.0. In contrast, *hb*PG possesses a partially branched structure, comprising both dendritic and linear units. The diverse topologies of polyglycerol allow for controlled hydrogen bonding with water through its unique 3D structure, demonstrating significant potential across various fields.[32,33] For example, we reported, by precisely controlling the degree of branching (DB) of PG, even a single type of *hb*PG can either promote or inhibit ice growth and recrystallization as its concentration varies and influences the extent of hydrogen-bonding formation with pure water molecules.[34,35] The design of polyglycerol species needs to be developed better in order to extend their effectiveness in ice-growth

T. K. Won, S. Y. Lee, D. J. Ahn
Department of Chemical and Biological Engineering
Korea University
Seoul 02841, Republic of Korea
E-mail: ahn@korea.ac.kr
A. Shin, B.-S. Kim
Department of Chemistry
Yonsei University
Seoul 03722, Republic of Korea
E-mail: bskim19@yonsei.ac.kr
D. J. Ahn
KU-KIST Graduate School of Converging Science and Technology
Korea University
Seoul 02841, Republic of Korea

The ORCID identification number(s) for the author(s) of this article can be found under https://doi.org/10.1002/adma.202416304

DOI: 10.1002/adma.202416304

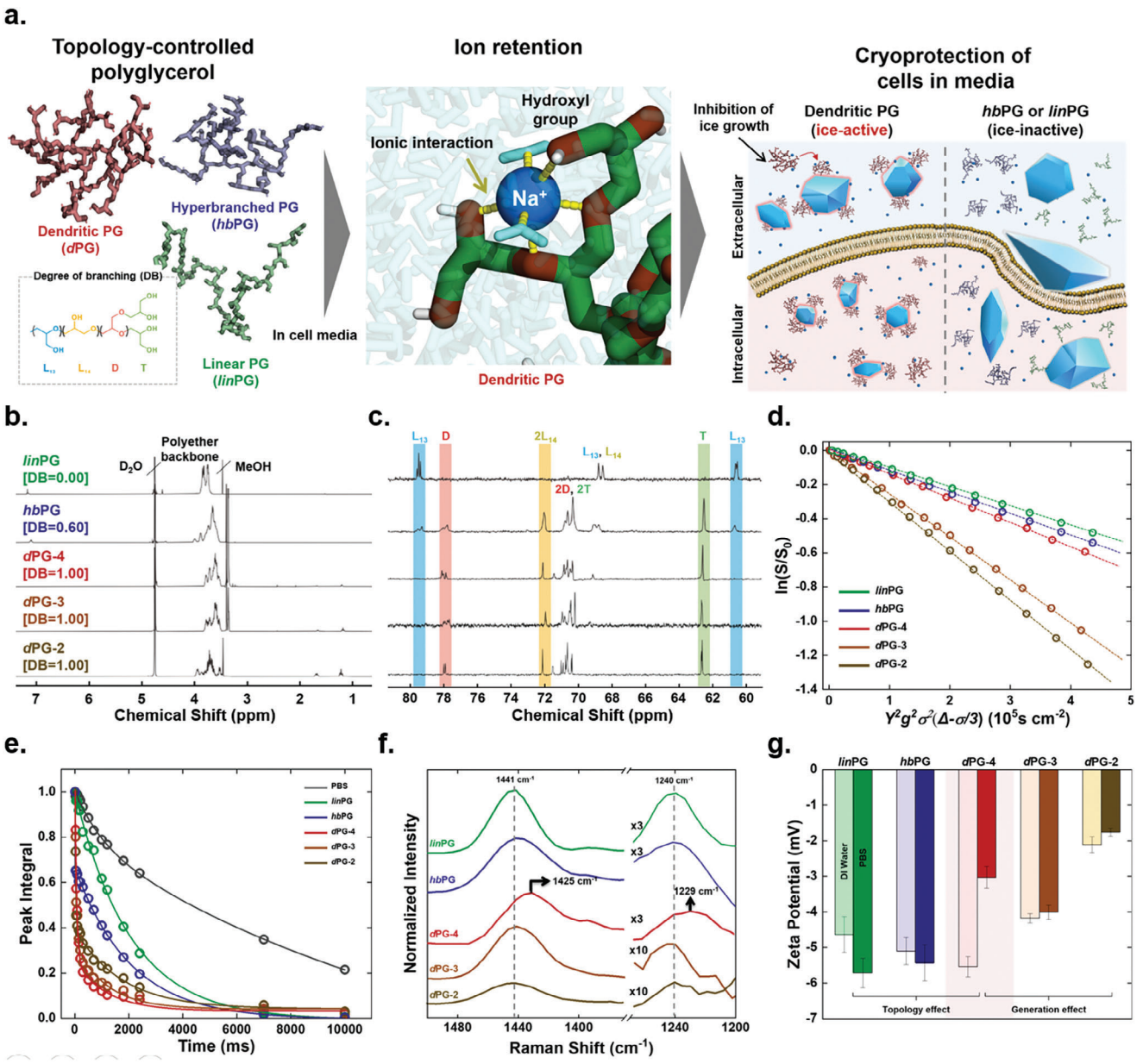

Figure 1. Material characterization of PGs by topology control. a) Schematic illustration of the cryoprotective dendritic polyglycerol and their preservation mechanism. The inset illustrates the assignment of the DB with linear (L_{13}, L_{14}), dendritic (D), and terminal (T) units. b) ^{1}H NMR (400 MHz, D_2O) and (c) ^{13}C NMR spectra (101 MHz, D_2O) of *d*PG, *hb*PG, and *lin*PG. d) ^{1}H DOSY NMR spectra of PGs in DI water. e) NMR spin-spin relaxation (T_2) curve of PG solutions in PBS buffer. f) Raman spectra of PGs in PBS. g) Zeta-potential of PGs in DI water (left bars) and PBS buffer (right bars).

activity to biological media, which is crucial in various coldchain of bio entities.

In this study, we report on a dendritic polyglycerol through the control of both topology and generation that exhibits ice growth inhibition in buffer media. By utilizing PGs with different topology by varying DBs (i.e., dendritic, hyperbranched, and linear), we assess the ice inhibition capacity facilitated through sodium ion retention by densely-packed arrays of hydroxyl and ether groups (**Figure 1a**). This approach provides a new design concept for polymeric materials to be effective for cell cryopreservation and the maintenance of network functionality in biological media.

2. Results and Discussion

2.1. Materials Characterization of PGs by Topology Control Under Media Conditions

We calculated the DB of the synthesized *d*PG, *hb*PG, and *lin*PG from the structural units of the linear (L_{13}, and L_{14}), dendritic (D),

Table 1. Number of oxygen group in ether/alcohol, molecular weights, GPC, diffusion coefficient (D), T_2 decay, and correlation time (τ) of *d*PGs, *hb*PG, and *lin*PG.

	Number of oxygen in ether/alcohol	$M.W._{theo}$	$M_{n,GPC}$	DB	D [10^{-6} m^2 s^{-1}]	T_2 [ms]	τ [ns]
*lin*PG	45 / 46	3439.71	3600[a)]	0.00	1.146	2045	0.018
*hb*PG	46 / 46	3485.72	3500[a)]	0.60	1.313	1986	0.019
*d*PG-4	42 / 48	3465.75	–	1.00	1.497	115 / 983	0.334 / 0.038
*d*PG-3	18 / 24	1689.83	–	1.00	2.950	109 / 2173	0.353 / 0.017
*d*PG-2	6 / 12	800.89	–	1.00	3.379	309 / 2674	0.122 / 0.014
PBS	–	–	–	–	–	3580	0.010

[a)] Determined from GPC measurements (DMF, RI signal, and PEG standard).

and terminal (T) groups present in the PGs (Figure 1b; Figure S1, Supporting Information). These structures were thoroughly analyzed using ^{1}H and ^{13}C nuclear magnetic resonance (NMR) spectroscopy. In ^{1}H NMR spectra, similar signals could be observed around 3–4 ppm, indicating that all five types of PGs shared similar polyether backbones (Figure S2, Supporting Information). However, ^{13}C NMR spectra clearly showed distinct peaks corresponding to the different structural units, confirming the varying DB values: 1.00 for *d*PG, 0.60 for *hb*PG, and 0.00 for *lin*PG (Figure 1c). The presence of dendritic and terminal units was further validated by the inverse-gated ^{13}C NMR technique, emphasizing the successful synthesis of perfectly branched dendritic structures. The unique multi-generational structure of dendrimers like *d*PG, resulting from sequential allylation and dihydroxylation steps, was corroborated using MALDI-ToF analysis (Figure S3, Supporting Information).

To investigate the solution behavior of these PGs as a function of their DB, diffusion-ordered NMR spectroscopy (DOSY) was performed (Figure 1d; Figure S4, Supporting Information). The DOSY results illustrate the diffusion coefficients (D) of *d*PG, *hb*PG, and *lin*PG in deionized (DI) water. The diffusion coefficient of *d*PG-4 was 1.497×10^{-6} m^2 s^{-1}, indicating a higher diffusion coefficient compared to *hb*PG and *lin*PG (**Table 1**). This is consistent with the theory that a higher DB in polyglycerol decreases hydrodynamic volume, leading to higher diffusion coefficients.[34,35] In addition, the lower the generation of *d*PG, the smaller the molecular weight of the dendrimer, resulting in an increase in the diffusion coefficient (Figure S5, Supporting Information). The mobility of water molecules in PBS was examined using proton spin-spin relaxation time (T_2) measurements of water (Figure 1e). Echo decay curves fitted with a biexponential function revealed two T_2 values for *d*PG-4 (115 and 983 ms), while *hb*PG and *lin*PG exhibited single T_2 values (1986 and 2045 ms, respectively).[36,37] Water dynamics, described by the correlation time (τ) calculated using the Bloembergen–Purcell–Pound equations, showed that *d*PG-4 had τ values of 0.334 and 0.038 ns, higher than *hb*PG and *lin*PG. It is noted that the dendritic structures all exhibited two hydrodynamic correlation times (τ); these τ values decreased as the generation increased. As a result, *d*PG-4 induced the least mobility of surrounding water molecules among PGs examined.

The interactions of PGs with media were monitored using Raman spectra (Figure 1f; Figure S6, Supporting Information). In DI water, all PGs exhibited similar peaks, with the C—O stretching vibration peak at 1240 cm−^{1} and the C—H bending vibration peak (methylene group adjacent to an oxygen atom) at 1441 cm^{-1} (Figure S6, Supporting Information). By contrast, a stark difference was observed in PBS; only the Raman peaks of *d*PG-4 were shifted lower to 1229 cm^{-1} for the C—O peak and 1425 cm−^{1} for the C—H peak, respectively. These shifts suggest that the hydroxyl and ether groups in *d*PG-4 engage in interactions with Na^+ ions inducing molecular vibrational dampening.[38,39] Notably, no interactions were observed in both *d*PG-3 and *d*PG-2. This ionic interaction of *d*PG-4 also influenced its zeta potential (**Figure 2g**). In DI water, *d*PG-4 exhibited a zeta-potential of −5.54 ± 0.28 mV, which decreased to −3.03 ± 0.31 mV in PBS, indicating a reduction in negative charge due to the presence of Na^+ ions. However, other PGs exhibited similar values of zeta potential with and without PBS buffer. These findings suggest that the precise molecular design provided the dense arrangement of hydroxyl and ether groups, which enabled interactions with Na^+ ions.

2.2. Evaluation of the Effect of PGs on Ice Recrystallization

We investigated the effects of PGs' topology and generation on ice recrystallization inhibition (IRI) in biological media. Ice recrystallization analysis was conducted using the splat method utilizing cross-polarized optical microscopy (POM) images after annealing at −6 °C for 30 min (Figure 2a; Figure S9, Supporting Information). PGs were found to be localized in the grain boundaries of ice crystals during the recrystallization process (Figure S10, Supporting Information). Evidently, the 4th generation *d*PG-4 formed smaller ice crystal sizes compared to other PGs. To quantify the observed results, the mean largest grain size (MLGS) was calculated based on the POM images (Figure 2b; Figure S11, Supporting Information). First, we examined the topology effect in PBS 1X (Figure 2b, upper panel) by comparing the cases of *d*PG-4, *hb*PG, and *lin*PG. MLGS values of *d*PG-4 were 39.6 ± 3.0 μm at 10 mM, 51.1 ± 3.0 μm at 1 mM, 62.7 ± 3.8 μm at 1 μM, and 68.7 ± 3.5 μm at 1 nM, indicating its ability to inhibit ice recrystallization. By contrast, *hb*PG exhibited 50.8 ± 6.3 μm

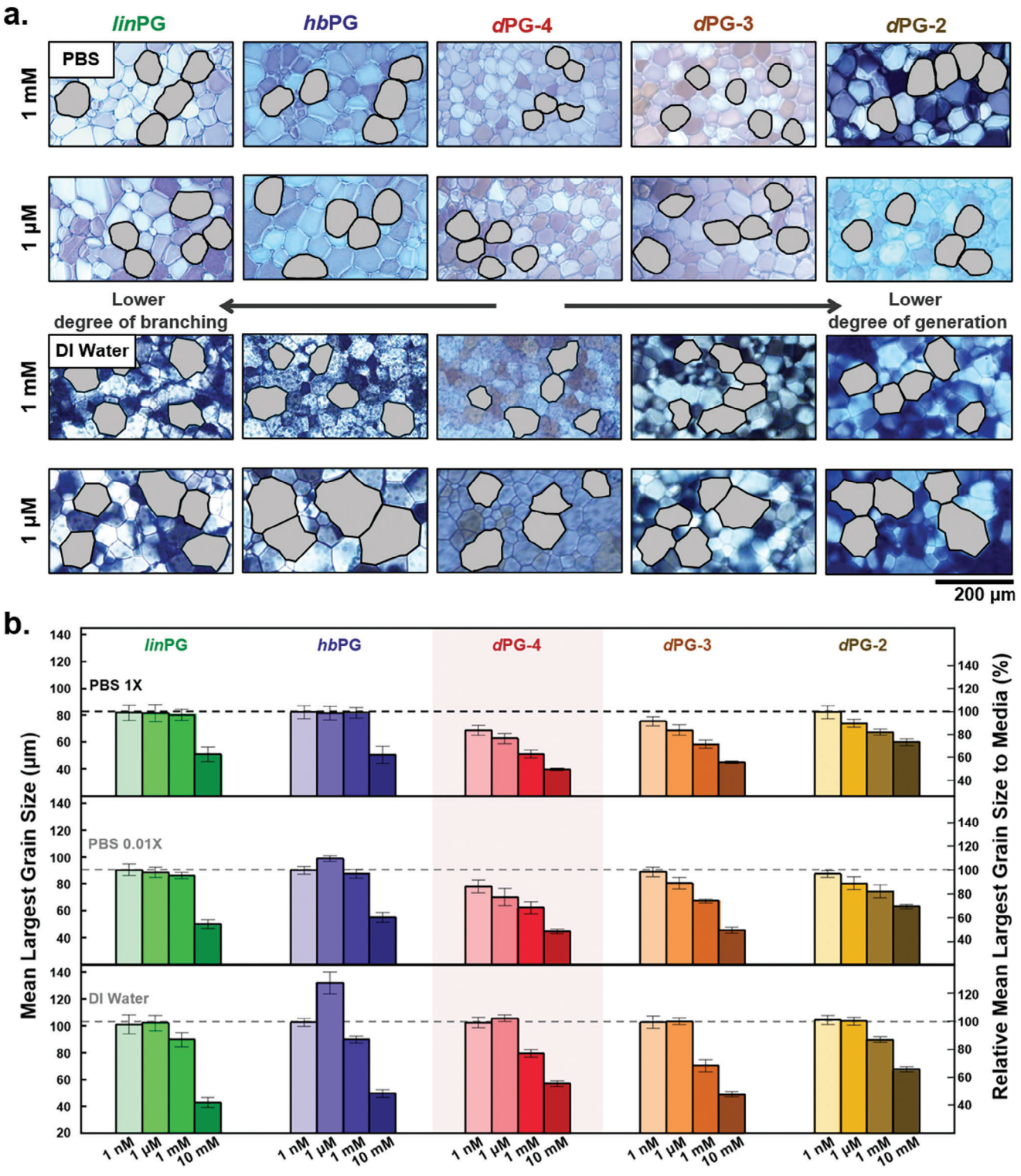

Figure 2. Evaluation of the effect of PGs on ice recrystallization. a) Cross-polarized optical microscopic images (POM) of PGs according to the topology in 1× PBS buffer after 30 min of annealing at −6 °C after splat-freezing at −196 °C. Marked areas represent five largest ice crystals per panel for eye-guiding purpose. b) Experimental results of ice recrystallization inhibition (IRI) of three types of PGs in PBS (1×, 0.01×) and DI water. IRI from *lin*PG (green), *hb*PG (blue), *d*PG-4 (red), *d*PG-3 (rust), and *d*PG-2 (olive). The PBS used was at a 1× concentration. Error bars indicate the standard deviation ($n = 5$).

at 10 mM, followed by 81.8 ± 4.1 μm, 81.6 ± 5.1 μm, and 82.3 ± 4.9 μm at lower concentrations. *lin*PG likewise showed 51.0 ± 5.5 μm, 80.1 ± 4.1 μm, 81.6 ± 6.5 μm, and 81.8 ± 5.5 μm with decreasing concentration. Both *hb*PG and *lin*PG lost IRI activity in PBS 1X at concentrations below 10 mM. Second, we examined the generation effect by comparing dendritic PGs (*d*PG-4, *d*PG-3, and *d*PG-2). In PBS 1X, MLGS values of *d*PG-3 were 45 ± 1.0 μm at 10 mM, 58.5 ± 3.0 μm at 1 mM, 69.0 ± 3.8 μm at 1 μM, and 75.5 ± 3.5 μm at 1 nM, indicating IRI activity lower than that of *d*PG-4. Even lower IRI activity was found for *d*PG-2. It is interesting to note that increased DB and higher generation of dendritic PG result in intensified IRI activity.

Next, we evaluated the effect of ionic strength using DI water, PBS 0.01X in addition to PBS 1X (Figure 2b, lower panels). When dissolved in DI water, *lin*PG, *hb*PG, and *d*PG-4 at 1 nM exhibited MLGS values similar that of pure water. At 1 μM, *d*PG-4 and *lin*PG showed relative MLGS values of 101.5 ± 2.5% and 98.3 ± 5.4%; respectively, while *hb*PG showed a value of 127.0 ± 7.9% indicating ice recrystallization promotion.[34] At 1 and 10 mM, all PGs displayed certain degree of IRI effects. Remarkably, In PBS 0.01X, dendritic PGs of all generations revealed better IRI activities than in pure water, unlike the cases of *lin*PG and *hb*PG. This trend became more intensified in the media having higher ionic strength, PBS 1×. Overall, these results suggest the possibility that there exists a relation of *d*PG-4's unique ability to complex Na^+ ions (Figure 1f,g) to the pronounced IRI activities as media's ionic strength increased (Figure 2b).

2.3. Molecular Dynamic Behavior of PGs in NaCl Aqueous Solution

We conducted all-atom (AA) molecular dynamics simulations to elucidate the mechanism by which the molecular structure of *d*PG overcomes the buffer effect and effectively inhibits ice recrystallization. Directional ice growth simulations have been used to theoretically evaluate the ice recrystallization performance of materials.[17,24] These simulations were generally performed using pure water as the medium. To consider the effect of the buffer, we configured the directional ice growth simulation system in a 137 mM NaCl solution, equivalent to the main component of 1× PBS buffer. The ice crystal seed plane consisting of two layers was exposed to the liquid phase on the secondary prism plane, known as the fastest growing plane.[40] To investigate the influence of the 3D molecular structure of PG, we used a linear structure with a DB of 0.00, a hyperbranched structure with a DB of 0.60, and a dendrimer structure with a DB of 1.00. To eliminate the initial impact between PG and the ice surface, PG was placed 2 nm away from the ice surface. All simulations were conducted at 267 K, where recrystallization actively occurred, for 200 ns.

As shown in **Figure** 3a, differences were observed depending on the presence and form of PG. In the case of NaCl without any material, 13 layers of ice grew over 200 ns. Interestingly, in the NaCl solution, only Cl^- ions were embedded in the ice as it grew. This specific engulfment of ions occurred due to the arrangement of surrounding water molecules influenced by the hydration shell of the ions, which matched the ice lattice. In contrast, when *d*PG-4 was present, ice growth was inhibited, resulting in only six layers of ice growing. During this process, *d*PG-4 adhered to the ice, forming hydrogen bonds with water molecules and creating a convex curvature on the surface, which inhibited ice growth through the Gibbs–Thomson effect. Remarkably, this ice growth inhibition was observed only with *d*PG-4 and not with *lin*PG or *hb*PG. In addition, the density profile in Figure 3a shows that only *d*PG-4 was located at the ice surface, with a high ion density at the interface. In contrast, *hb*PG and *lin*PG were found in the bulk water and were pushed away from the ice front as the ice grew. As a result, *d*PG-4 allowed only 1.5 nm of ice growth over 200 ns, whereas *hb*PG and *lin*PG allowed 4 nm of growth, similar to the NaCl solution without any additives (Figure 3b). This indicates that *lin*PG and *hb*PG had no significant effect on inhibiting ice growth in salt water.

Next, we quantified the interaction of PGs with Na^+ ions and found a strong ionic retention by *d*PG-4 (Figure 3c). *d*PG-4 retained up to eight ionic interactions with Na^+, which was 2.7 times higher than *hb*PG and 7.2 times higher than *lin*PG. Notably, in the period from 30 to 80 ns (highlighted by the gray shadow in the figure), where *d*PG-4 formed numerous retentions with Na^+, the number of hydrogen bonds with ice significantly increased (Figure 3d). These results indicate that *d*PG-4 captures many Na^+ ions around it, and such a dendritic structure allows it to form hydrogen bonds with the ice. The retention process of Na^+ ions by *d*PG-4 was observed at the molecular level. In the hydration shell of Na^+, up to four of the six water molecules were replaced by ionic interactions with *d*PG-4, keeping Na^+ ions around it for an extended period, unlike lower generation dendrimers (Figure 3e; Figure S12, Supporting Information). As shown in Figure 3f, *d*PG-4 carrying Na^+ ions could easily approach the ice being relatively negative-charged. *d*PG-4 then adhered to the ice surface and formed hydrogen bonds; while, Na^+ ions were pushed away from the ice and afterward located in the bulk water.

2.4. Cryoprotective Activity of HSC-3 Cells and Retardation of Intracellular Ice Growth

We assessed the potential application of *d*PG-4, which demonstrated IRI in PBS buffer, for cell cryopreservation. PG used as drug delivery vehicles could be internalized by cells via endocytosis, with polymer structure and cell type known to influence uptake efficiency.[30] Using confocal microscopy to observe the cellular uptake behavior of PG, we found that the fluorescence intensity of Cy5-conjugated *d*PG-4 within human tongue squamous carcinoma (HSC-3) cells decreased by 34.0% after 1 h of incubation and by 41.1% after 2 h, compared to *lin*PG. This indicates that as DB (from linear to dendritic) increases, cellular uptake efficiency decreases (**Figure** 4a; Figure S13, Supporting Information). Next, we evaluated the cryoprotective performance of the three PGs using the 3-(4,5-dimethylthiazol-2-yl)-2,5-diphenyltetrazolium bromide (MTT) assay. After cryopreservation, the cells were quickly thawed at 37 °C, and all samples were replaced with PBS buffer for the MTT assay, which was completed within 30 min post-thawing. After 1 day of cryopreservation, 10% DMSO achieved a survival rate of 59.9 ± 3.2%. Without a cryoprotectant, survival was 51.9 ± 5.9% relative to 10% DMSO. In contrast, 1 mM of *d*PG-4, *hb*PG, and *lin*PG showed the relative

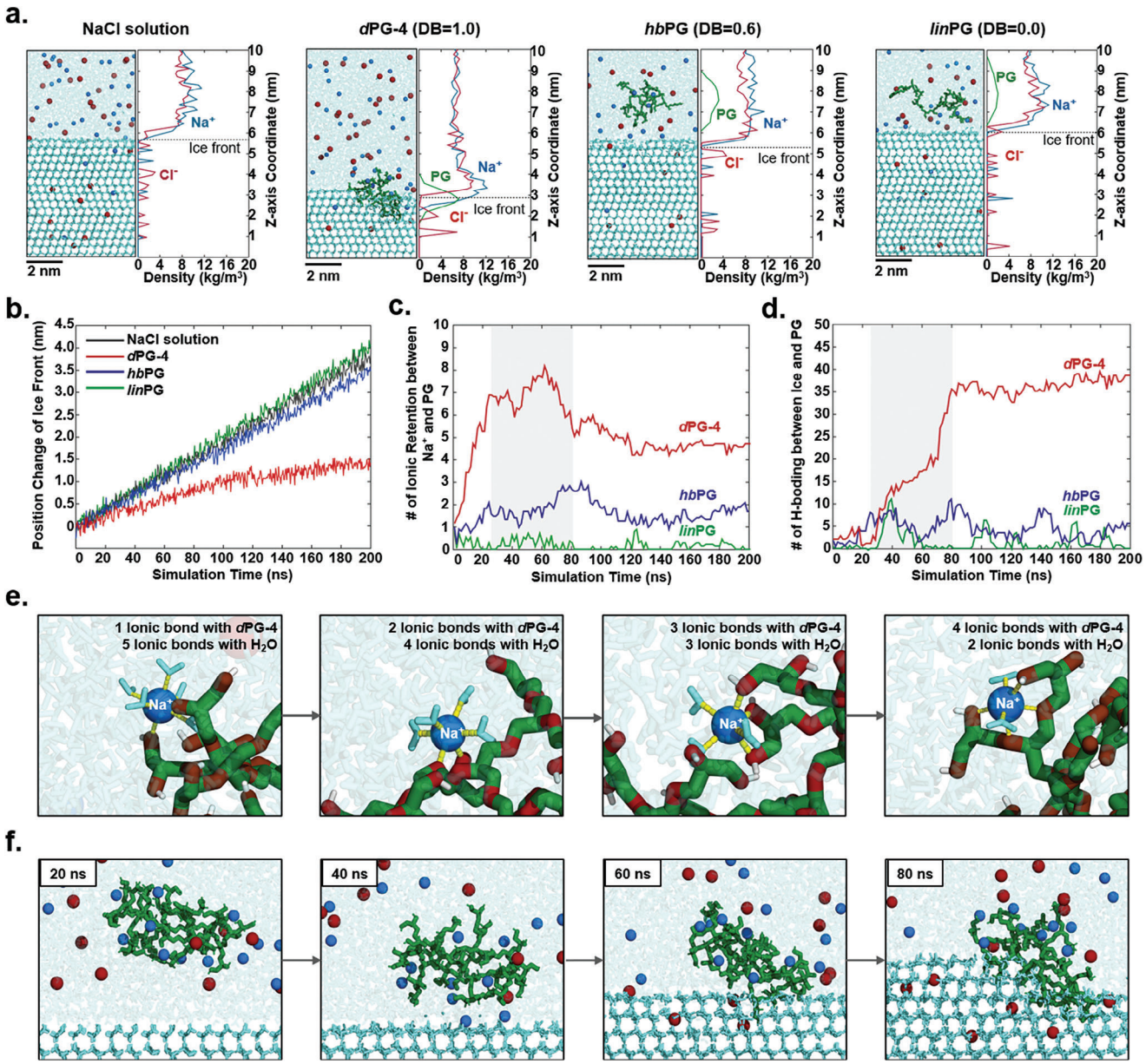

Figure 3. Molecular dynamic behavior of PGs with respect to DB in NaCl aqueous solution. a) Ice growth simulation results and density profiles against *z*-axis in NaCl solution (first panel), *d*PG-4 (second panel), *hb*PG (third panel), and *lin*PG (fourth panel). b) Measurements of the time-dependent positional changes of the ice front. c) Time-dependent ionic coupling between PGs and Na^+. d) Changes in the number of hydrogen bonds between PGs and the ice surface over time. e) Ionic coupling process between Na^+ ions and *d*PG-4. f) Molecular dynamic snapshots showing the effect of Na^+ ions trapped by *d*PG-4 on ice growth. Liquid water, PGs, sodium ion, and chloride ion are represented by transparent cyan, green, blue, and red colors, respectively (a,f).

survival rates of 133.6 ± 21.2%, 61.8 ± 5.0%, and 73.1 ± 10.4%, respectively. Notably, *d*PG-4 maintained its cryoprotective effect even after 1 week, with a survival rate of 135.1 ± 8.3% compared to 10% DMSO (Figure 4b). Extended incubation to 2 h slightly decreased survival, indicating that 1-h incubation at 1 mM was optimal (Figure S14, Supporting Information). Higher concentrations (10 mM) showed cytotoxicity; while, lower concentrations-maintained cell viability (Figure S15, Supporting Information).

To further deepen the mechanistic understanding behind the superior cryoprotective performance of *d*PG-4, we observed intracellular ice growth. Intracellular ice formation and growth are known to adversely affect cell viability.[26] Cells stained with a sodium indicator displayed black dots representing ice particles as the dye molecules were excluded from the ice crystals. The results showed that *d*PG-4 inhibited intracellular ice crystal growth, resulting in numerous small ice crystals. Qualitative comparison revealed that the size of intracellular ice crystals was smallest in *d*PG-4-treated cells, followed by *lin*PG, *hb*PG, and non-treated cells (Figure 4c; Figure S16, Supporting Information). Quantitatively, the number of ice crystals and the ice fraction relative

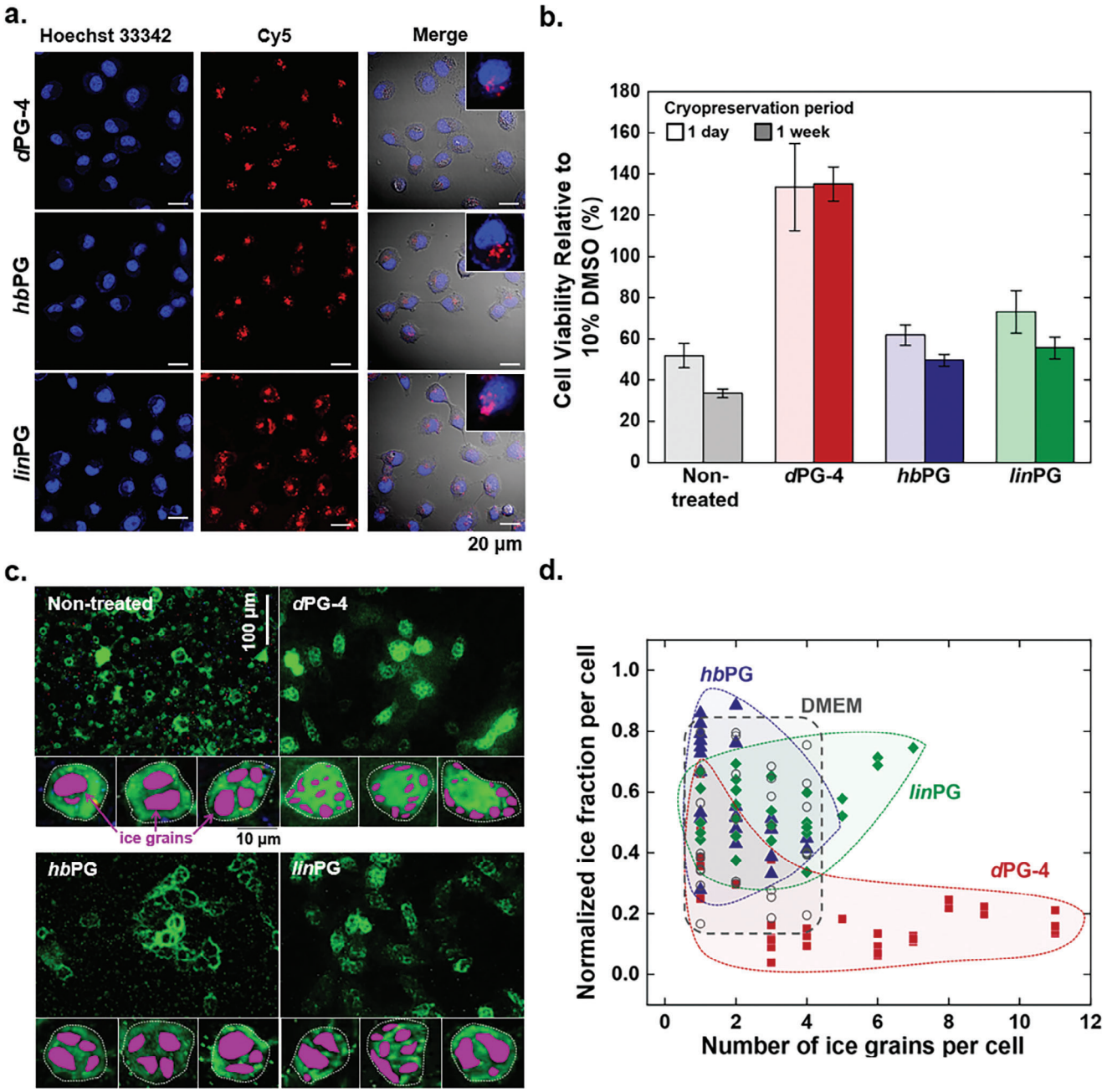

Figure 4. Cryopreservation of HSC-3 cells using various PGs and their effects on intracellular ice formation. a) Confocal fluorescence microscopy images of HSC-3 cells after Hoechst dye 33342 (blue) pre-treatment with PGs labeled with Cy5 (red) for 1 h. b) MTT assay after cryopreservation of the cells treated with PGs. All PGs were incubated for 1 h, except for 10% DMSO. Error bars indicate the standard deviation ($n = 5$). c) Wide-field fluorescence images of non-treated and PG-treated cells when elevated to −6 °C from −196 °C (detailed in Experimental Section). Green indicates the sodium indicator. Magenta in the insets does the intracellular ice grains formed. d) Distribution of the number and fraction of intracellular ice grains observed in (c). Each data point correspond to an individual cell. The concentration of PGs used is 1 mM.

to cell size were assessed. The normalized ice fraction was calculated using the cell area at −6 °C. Typically, as intracellular ice particles recrystallize, the ice fraction increases and the number of particles decreases, a pattern observed in control cells and those treated with *hb*PG. Although *lin*PG-treated cells sometimes showed a higher number of ice crystals than *hb*PG, they exhibited a higher ice fraction. However, *d*PG-4, which provided the highest post-thaw survival rates, displayed up to 11 intracellular ice crystals with a fraction below 0.4, indicating a noticeable delay or suppression in the coalescence of intracellular ice particles (Figure 4d, red symbol). Thus, *d*PG-4 not only inhibits extracellular ice formation but also effectively suppresses intracellular ice growth, even with lower cellular uptake efficiency, leading to enhanced cell survival.

2.5. Assessing In Vitro Tube Formation Capability of HUVEC Cells After Cryopreservation

Tube formation in HUVEC cells has served as a key model in vascular biology research. Tube formation requires a sufficient number of viable cells with intact membranes.[41,42] Traditionally, HUVEC networks are established after at least two passages of cells stored in liquid nitrogen.[41] We explored whether the high cell viability with *d*PG-4 influences HUVEC tube formation. After 1 day of cryopreservation, *d*PG-4 achieved a survival rate of 146.7 ± 15.3% relative to 10% DMSO (**Figure 5**a; Figure S17, Supporting Information).

As shown in Figure 5b, the parameters used to detect and quantify tube network formation include the number of nodes, tubes, and meshes. Initial HUVEC cell tube formation yielded 333 ± 40 nodes, 56 ± 8 tubes, and 30 ± 6 meshes. Further, we confirmed that 10% DMSO, *d*PG-4, *hb*PG, and *lin*PG do not inhibit tube formation (Figure S18, Supporting Information). We assessed tube formation immediately after replacing the medium with fresh media for cryopreserved cells for 1 day (Figure 5c). The results revealed that cells cryopreserved with 10% DMSO showed disconnected nodes, tubes, and meshes, and both *hb*PG and *lin*PG predominantly failed to form tubes from the nodes possibly, due to low viability. Notably, the extent of the HUVEC network after cryopreservation with *d*PG-4 was significant (Figure 5c; Figure S19, Supporting Information). The nodes, tubes, and meshes were arranged similarly to the initial state, suggesting that the surviving cell number and membrane integrity were adequate for network formation. The quantification showed that *d*PG-4 maintained 90.4 ± 7.5% of nodes, 92.9 ± 17.9% of tubes, and 84.4 ± 28.1% of meshes relative to the initial HUVEC network, demonstrating its ability to preserve tube formation compared to 10% DMSO (Table S1, Supporting Information). This suggests that the unique properties of biocompatible *d*PG-4, such as ion retention, effectively inhibit the growth of intracellular and extracellular ice crystals and mitigate osmotic shock due to ion concentration, thereby securing high cell viability and membrane integrity.

3. Conclusion

The fourth generation of dendrimer *d*PG-4 demonstrated a significant ice inhibition activity in biological media containing ample ions, whereas *hb*PG and *lin*PG counterparts exhibited no such effect. We elucidated that the molecular structural details influence interactions of PGs with ions dissolved. Specifically, the well-controlled dendritic molecular structure of *d*PG-4 induced Na^+ ion retention, which facilitated the polymer to form hydrogen bonding with the ice surface; *d*PG-4 carrying Na^+ ions could easily approach the negatively charged ice; and then, adhered to the ice surface; while, Na^+ ions were pushed away from the ice. This mechanism activated *d*PG-4 to inhibit ice growth and recrystallization. Such cell-permeable *d*PG-4 functioned in both intracellular and extracellular spaces, whereas *hb*PG and *lin*PG, also permeable, inhibited little intracellular ice growth. As a result, *d*PG-4 achieved remarkable cryoprotective effects on the recovery of cells (≈134–147% relative to 10% DMSO), and the post-thaw functionality of tube formation (≈90% for nodes, ≈93% for tubes, and ≈84% for meshes). This discovery suggested a new design strategy for polymers as potent cryoprotective materials, which is expected to impact the current preservation technologies for various biological entities.

4. Experimental Section

Materials: 1,1,1-Tris(hydroxymethyl)propane, benzyl alcohol, glycidol, N-methyl-2-pyrrolidone (NMP), tetrabutylammonium bromide, *p*-toluenesulfonic acid monohydrate, osmium tetroxide (4% in water), and t-butanol were purchased from Sigma–Aldrich. Allyl chloride, ethyl vinyl ether, and N-methylmorpholine N-oxide (NMO) were purchased from Tokyo Chemical Industry. 50 wt% sodium hydroxide and sodium sulfate were purchased from Samchun. Acetone, hexane, ethyl acetate, toluene, and methanol were purchased from the SK chemical.

Synthesis and Characterization of Dendritic Polyglycerols (dPGs): Dendritic polyglycerols (*d*PGs) were synthesized by a two-step process based on sequential allylation and dihydroxylation. The values from each carbon unit were integrated using the formula:

$$\mathrm{DB} = \frac{2\mathrm{D}}{2\mathrm{D} + L_{13} + L_{14}} \quad (1)$$

The DB of PGs was calculated to confirm its partially branched structure.

Allylation: In a one-neck flask, polyol (0.10 mol, alcohol equiv) tetrabutylammonium bromide (3.23 g, 0.01 mol), 50 wt% sodium hydroxide (40 g, 0.50 mol), and allylchloride (40.7 mL, 0.50 mol) were added over 22 h at 45 °C under vigorous stirring. After the reaction was completed, the reaction mixture was separated into an organic phase and an aqueous phase through extraction, followed by drying over $MgSO_4$, filteration, and concentrating in vacuo. The crude product was further purified by column chromatography (silica gel, hexane:ethyl acetate 16:1 to 2:1) to obtain a colorless oil.

Dihydroxylation: In a one-neck flask, polyallyl ether (0.10 mol, allyl equiv.) and *N*-methylmorpholine *N*-oxide (14.8 g, 0.11 mol) were added to a mixture of acetone (50 mL), distilled water (50 mL), and t-butanol (10 mL). Osmium tetroxide (4% in water) was added and stirred for 20 h at room temperature. Then, all volatile compounds were removed in vacuo. The crude product was further purified by column chromatography (silica gel, ethyl acetate:methanol 4:1 to 1:1). The high-molecular weight dendritic polyglycerols (*d*PG-3 and *d*PG-4) were purified by dialysis in methanol using cellulose membrane (MW 1000, Sigma). After concentration, yellow oils were obtained. Successful synthesis of *d*PG-4 was confirmed by ^{1}H, ^{13}C NMR, and MALDI-ToF. ^{1}H NMR (400 MHz, D_2O): δ [ppm] 0.86 (*t*, 3H, CH_3), 1.39 (*q*, 2H, CH_2CH_3), and 3.43–3.72 (*m*, 231H). ^{13}C NMR (101 MHz, D_2O) δ 78.09, 77.86, 72.06, 71.39, 70.79, 70.59, 70.42, 70.30, 70.27, 69.06, and 62.50.

Synthesis of Linear and Hyperbranched Polyglycerols: The polymer was prepared according to the method described in the authors' previous study.[34] Successful polymerization of *lin*PG and *hb*PG was confirmed by ^{1}H, ^{13}C NMR, and GPC. *hb*PG: ^{1}H NMR (400 MHz, D_2O): δ 7.39 (s, 5H), 4.56 (s, 2H), and 3.49–3.95 (m, 239H). ^{13}C NMR (101 MHz, D_2O): δ 79.43 (d, J = 24.4 Hz), 77.80, 71.98, 70.95–69.83 (m), 68.85 (d, J = 26.7 Hz), 62.43, 60.59. ($M_{n,NMR}$: 3500; $M_{n,GPC}$: 3300; M_w/M_n: 1.17) *lin*PG: ^{1}H NMR (400 MHz, D_2O): δ 7.46 (m, 5H), 4.63 (s, 2H), and 3.82–3.65 (m, 230H). ^{13}C NMR (101 MHz, D_2O): δ 128.65, 128.41, 79.64, 79.55, 79.44, 68.79, 68.54, 60.59, 60.49, and 48.73 ($M_{n,NMR}$: 3600; $M_{n,GPC}$: 3500; M_w/M_n: 1.08).

^{1}H DOSY NMR Experiments: All PG samples, including *d*PG, *hb*PG, and *lin*PG, were individually prepared at a concentration of 1.0 mM in D_2O. Diffusion coefficient measurements were carried out using pulsed-field-gradient DOSY NMR experiments with a maximum gradient strength of 52.9 mT m^{-1}. The diffusion gradient length (δ) of 2.0 ms delayed stabilizing the gradients, and the magnetic field gradient amplitudes were incrementally increased from 2.10×10^{-2} to 5.2×10^{-1} T m^{-1} in a linear ramp. For each gradient amplitude, 16 transients were recorded with 16 384

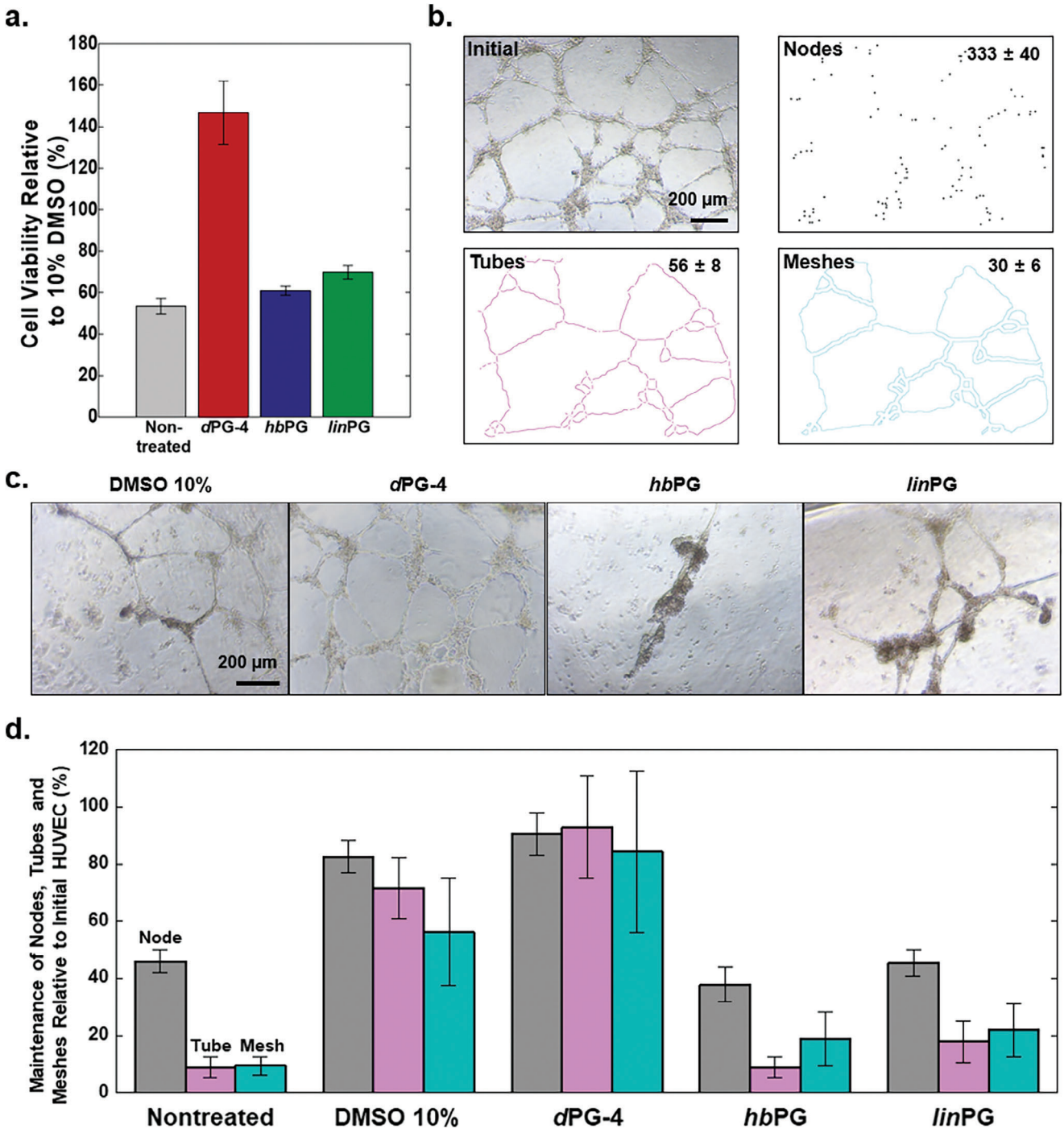

Figure 5. HUVEC network formation after cryopreservation using various PGs. a) MTT assay after cryopreservation for 1 day of the cells treated with various PGs. All PGs were incubated for 1 h, except for 10% DMSO. b) Optical image after HUVEC network before cryopreservation and corresponding images detected using NIH Image) software with angiogenesis plugins for total nodes (grey), tubes (magenta), and meshes (cyan), respectively. The numbers represent the average counts and standard deviations of nodes, tubes, and meshes. c) Optical images of network formation of the cells after cryopreservation with various treatments and d) their quantified assessment of tube formation. The concentration of PGs used is 1 mM. Error bars of (a,d) indicate the standard deviation ($n = 5$).

complex data points, resulting in a total experimental duration of 16 min. The diffusion gradient length (δ) was set to 2 ms for the diffusion time, with a diffusion delay of 20 ms. The NMR data were analyzed, and diffusion coefficients (D) were calculated using the DOSY Toolbox software package. The diffusion experiments exhibited an error of ≈1.8%, primarily due to variability in data acquisition reproducibility. The signal attenuation induced by the gradients was determined by fitting the Stejskal–Tanner equation through DOSY analysis.

$$S = S_0 exp\left(D - \gamma^2 G^2 \delta\left(\Delta - \frac{\delta}{3}\right)\right) \quad (2)$$

where S was the signal amplitude as a function of gradient strength g, S_0 was the signal amplitude at $g = 0$, D was the diffusion coefficient, γ was the proton gyromagnetic ratio, δ was the gradient pulse duration, and Δ was the diffusion time.

Ice Recrystallization Experiment: To analyze RI activity, the splat-freezing method was employed. A 10 µL of sample was rapidly frozen by dropping it onto a glass substrate pre-cooled with liquid nitrogen (at −196 °C). The frozen sample was then annealed at −6 °C for 30 min on a temperature-controlled microscope stage and observed. After 30 min, the average size of the ten largest ice domains was measured and compared to that obtained using PBS or DI water to estimate the mean largest grain size (MLGS). The MLGS values reported were calculated from six independent observations.

NMR Spin–Spin Relaxation (T_2) Measurements for Water in PGs Samples: The spin–spin relaxation time (T_2) of water in polyglycerol (PG) samples was measured using a 400 MHz NMR spectrometer (model 400JJYH, ZEOL) with the Carr–Purcell–Meiboom–Gill (CPMG) pulse sequence. The interval between the 90° and 180° pulses was set at 1.2 ms. To achieve complete magnetization recovery between scans, the spin-lattice relaxation time was adjusted to be at least ten times longer than the T_1 relaxation time. A mixture of PG solution and dipotassium deuterated PBS buffer in a 1:99 volume ratio was prepared and placed in an NMR tube. The T_2 relaxation behavior of the water protons was analyzed by fitting the acquired data to a biexponential decay model.[43]

$$E_t = f_{2,a} exp\left(-\frac{t}{T_{2,a}}\right) + f_{2,b} exp\left(-\frac{t}{T_{2,b}}\right) + E_0 \quad (3)$$

The dynamic of water could be represented by the correlation time for the motion of water (τ_c) by using the Bloembergen–Purcell–Pound equation as

$$\frac{1}{T_2} = \frac{C}{2}\left(3\tau_c + \frac{5\tau_c}{1+\omega_0^2\tau_c^2} + \frac{5\tau_c}{1+4\omega_0^2\tau_c^2}\right) \quad (4)$$

where C was a constant for water of 5.33×10^9 s^{-2} and ω_0 was the Larmor frequency.

Molecular Dynamics Simulation: All-atom molecular dynamics (MD) simulations were performed to investigate the mechanism by which *d*PG-4 overcame the buffer effect and inhibited ice recrystallization. Simulations were conducted using the GROMACS software package, with the CHARMM36 force field employed for the representation of *d*PG and the TIP4P/Ice water model for water molecules. The simulation system was prepared by placing the ice crystal in a cubic simulation box filled with 137 mM NaCl solution, which was representative of 1× PBS buffer. The ice crystal plane was oriented to expose the secondary prism plane to the liquid phase, known as the fastest growing plane. Three different structures of PG were used: linear PG (*lin*PG) with a DB of 0, hyperbranched PG (*hb*PG) with a DB of 0.6, and dendritic PG (*d*PG) with a DB of 1. To eliminate initial artificial interactions between PG and the ice surface, PG molecules were placed 2 nm away from the ice surface. The system was then solvated with water molecules, and Na^+ and Cl^- ions were added to achieve the desired ionic concentration. Energy minimization was performed to remove any bad contacts in the system. Equilibration of the system was carried out in two phases: the first phase involved a 100 ps NVT (constant number of particles, volume, and temperature) equilibration at 267 K using the V-rescale thermostat, followed by a 100 ps NPT (constant number of particles, pressure, and temperature) equilibration at 1 bar using the Parrinello–Rahman barostat. Production MD simulations were then conducted at 267 K for 200 ns with a time step of 2 fs. During the production run, various properties were monitored, including the number of ice layers formed, hydrogen bonding interactions, and the spatial distribution of ions and PG molecules. The retention of Na ions by PGs and their interactions with the ice surface were quantified by calculating the number of ionic interactions and hydrogen bonds over time. All simulations were performed using periodic boundary conditions to minimize edge effects. Long-range electrostatic interactions were calculated using the Particle–Mesh–Ewald (PME) method, with a real-space cutoff of 1.2 nm. van der Waals' interactions were truncated at 1.2 nm, and the LINCS algorithm was used to constrain bond lengths involving hydrogen atoms.

Cell Culture and Cryopreservation: HSC-3 cells were obtained from Sigma–Aldrich (USA). For all experiments, cells at passages 8 to 10 were used. The cells were cultured in Dulbecco's modified eagle's medium (DMEM) supplemented with 10% heat-inactivated fetal bovine serum (FBS) and 100 U mL^{-1} penicillin–streptomycin (Gibco, USA). Cells were maintained in 75 cm^2 tissue culture flasks at 37 °C in a humidified atmosphere with 5% CO_2. Cells were detached using trypsin-EDTA (Gibco), resuspended in fresh culture medium (15 mL), and subcultured every 48–72 h. Human umbilical vein endothelial cells (HUVEC) were acquired from American Type Culture Collection (ATCC, USA). Passages 2 to 6 were used throughout the experiments. HUVEC was cultured in Endothelial Cell Growth Medium-2 (EBM-2, Lonza, Switzerland) under similar conditions as described for HSC-3 cells.

The cryoprotective efficacy was assessed using the following cryopreservation protocol. Live cells cultured in T75 flasks were detached using EDTA. The resulting cell suspension was collected into a 15 mL conical tube and centrifuged to form a pellet, followed by replacing the supernatant with fresh medium. A solution of 10 µL DMSO or PGs was combined with 90 µL of a cell suspension containing 1.2×10^6 cells in fresh medium. The mixture was incubated at 37 °C in a 5% CO_2 humidified atmosphere for a designated time before freezing. For rapid cryopreservation, cells were quickly transferred to a liquid nitrogen chamber and stored for either 1 day or 1 week. After cryopreservation, thawing was performed in a 37 °C water bath for 2 min, followed by the MTT assay.

MTT Assay for HSC-3 and HUVEC Cells: Mitochondrial activity was evaluated using the MTT assay with a spectrophotometric approach. Immediately following warming, the cells were homogenized in PBS and incubated with 10 µL of MTT solution (conc. 100 µg mL^{-1}) added to 90 µL of HSC-3 or HUVEC cell culture medium. After a 2 h incubation at 37 °C, the medium was removed. To solubilize the formazan crystals, 100 µL of a 2% SDS solution (prepared in 0.01 M HCl, 10%) was added to each sample and incubated for 4 h at 37 °C without the addition of DMSO. The absorbance was then read at 570 nm using a microplate reader. Two-hundred microliters of fresh medium without cells served as the control, and the viability of cells prior to freezing was set as 100%.

Measurement of Intracellular Ice-Crystal Observation: To observe the formation of intracellular ice crystals, HSC-3 cells were stained with the sodium indicator CoroNa Green (emission maximum at 516 nm, final concentration of 1 µM). The stained cells were placed between two cover glasses in fresh medium and mounted on a temperature-controlled cold stage (THMS600; Linkam, UK). The samples were rapidly cooled at a rate of 150 °C min^{-1} to −196 °C and held at this temperature for 1 h. They were then reheated at a rate of 95 °C min^{-1}, allowing for the observation of intracellular ice crystals as the temperature reached −6 °C. The ice fraction per cell was calculated as the ratio of the area of intracellular ice crystals to the total cell area at −6 °C.

In Vitro Angiogenesis Assay for HUVEC Network: To establish the HUVEC network, the standard protocol provided by the In Vitro Angiogenesis Assay Kit (ECM625, Sigma-Aldrich) was followed. The supplied ECMatrix and Diluent Buffer were thawed on ice or in a 0 °C water bath, protected from light. A mixture of 100 µL of Diluent Buffer and 900 µL of ECMatrix was prepared and thoroughly mixed. Subsequently, 50 µL of this mixture was added per well of a 96-well tissue culture plate, ensuring even

distribution without air bubbles and incubated at 37 °C for over an hour to allow solidification. HUVEC cells, prepared as per standard cell culture procedures, were adjusted to a concentration of 1×10^5 cells mL^{-1}. Then, 50 µL of the medium containing HUVEC cells was added to each well containing the polymerized matrix and incubated in a 37 °C CO_2 incubator for over 10 h to promote angiogenesis. The identical protocol was followed by samples prepared for cryopreservation. Quantitative analysis of the network formation, including the number of nodes, tubes, and meshes, was conducted using the Angiogenesis Analyzer for ImageJ, as previously described.

Characterization: ^1H and ^{13}C nuclear magnetic resonance (NMR) spectra were obtained using an Agilent 400 MHz spectrometer at 298 K. Deuterated chloroform ($CDCl_3$) and deuterium oxide (D_2O) were employed as solvents, with tetramethylsilane (TMS) serving as the internal standard reference. Gel permeation chromatography (GPC) analyses were conducted on an Agilent 1200 series system, utilizing DMF as an eluent at 40 °C and a flow rate of 1.0 mL min^{-1}, with a refractive index (RI) detector. The GPC system was equipped with a PLgel 5 µm guard column and two PLgel 5 µm mixed-D columns (Agilent). Calibration was carried out using poly(ethylene glycol) (PEG) standards to determine the number-average (M_n) and weight-average (M_w) molecular weights. MALDI-ToF mass spectrometry (MS) measurements were performed by using trans-2-[3-(4-tert-butylphenyl)-2-methyl-2-propenylidene]malononitrile as a matrix on a Bruker Autoflex Max instrument.

Raman spectra were obtained using an inverted Raman microscope (NOST, South Korea) equipped with a 60× objective lens (0.6 N.A.) from Olympus (Tokyo, Japan). The sample solution was excited with a 543 nm laser (CNI laser, China). The scattered Raman signals were collected through a confocal motorized pinhole (100 µm) and directed to a spectrometer (FEX-MD, NOST, Korea) with a 1200 g mm^{-1} grating. The resulting spectra were captured using a spectroscopy charge-coupled device camera (Andor [DV401A-BVF], Belfast, Northern Ireland). For Fourier-transform infrared (FT-IR) spectroscopy, measurements were performed on an Agilent Cary 630 spectrometer equipped with an attenuated total reflection (ATR) module.

Ultraviolet–visible (UV–vis) spectroscopy was employed to quantify the release of cisplatin in PBS using a Shimadzu RF-6000 UV–vis spectrometer. The optical/fluorescence microscopy (BX51, Olympus). The surface charge was analyzed using electrophoretic light scattering spectroscopy (ELS-Z2, Otsuka Electronics). The live cell imaging was observed by confocal laser scanning microscopy (LSM700, Carl Zeiss). The MTT assay results were read at 570 nm using a Victor 5 multilabel plate reader (PerkinElmer). Fluorescence spectra were acquired with an Infinite 200 PRO multimode microplate reader (Tecan). Finally, confocal fluorescence microscopy was carried out to capture live cell images using a Zeiss LSM 800 microscope.

Supporting Information

Supporting Information is available from the Wiley Online Library or from the author.

Acknowledgements

This work was supported by the National Research Foundation of Korea under 2021R1A2C3009955, 2021R1A2C3004978, RS-2023-00214066, RS-2024-00507436, and RS-2024-00508678. The authors thank Yedam Lee (Korea University) for helpful discussions on intracellular ice analysis.

Conflict of Interest

The authors declare no conflict of interest.

Author Contributions

D.J.A. and B.-S.K. designed and supervised the project. T.K.W., A.S., and S.Y.L. contributed equally to this work. T.K.W., A.S., S.Y.L., B.-S.K, and D.J.A. prepared the initial draft of the manuscript. T.K.W. and A.S. performed the experiments and analyses. S.Y.L. and D.J.A. conducted MD simulation and mathematical analyses. All authors contributed to reviewing and editing of the manuscript.

Data Availability Statement

The data that support the findings of this study are available from the corresponding author upon reasonable request.

Keywords

cell cryopreservation, cellular network formation, ice-growth inhibition, molecular dynamic simulation, sodium-complexed polyglycerol

Received: October 24, 2024
Revised: December 10, 2024
Published online:

[1] P. Mazur, *Science* **1970**, *168*, 939.
[2] S. Giwa, J. K. Lewis, L. Alvarez, R. Langer, A. E. Roth, G. M. Church, J. F. Markmann, D. H. Sachs, A. Chandraker, J. A. Wertheim, M. Rothblatt, E. S. Boyden, E. Eidbo, W. P. A. Lee, B. Pomahac, G. Brandacher, D. M. Weinstock, G. Elliott, D. Nelson, J. P. Acker, K. Uygun, B. Schmalz, B. P. Weegman, A. Tocchio, G. M. Fahy, K. B. Storey, B. Rubinsky, J. Bischof, J. A. W. Elliott, T. K. Woodruff, et al., *Nat. Biotechnol.* **2017**, *35*, 530.
[3] A. Borini, G. Coticchio, *Preservation of Human Oocytes: From Cryobiology Science to Clinical Applications*, CRC Press **2009**.
[4] M. Lee, S. Y. Lee, M.-H. Kang, T. K. Won, S. Kang, J. Kim, J. Park, D. J. Ahn, *Nat. Commun.* **2024**, *15*, 908.
[5] N.-R. Park, Y. Lee, S. Y. Lee, H.-N. Kim, M.-K. Kim, D. J. Ahn, *Small Sci.* **2024**, *4*, 2400427.
[6] C. Polge, A. U. Smith, A. Parkes, *Nature* **1949**, *164*, 666.
[7] J. E. Lovelock, M. W. Bishop, *Nature* **1959**, *183*, 1394.
[8] J. Galvao, B. Davis, M. Tilley, E. Normando, M. R. Duchen, M. F. Cordeiro, *FASEB J.* **2014**, *28*, 1317.
[9] A. Fowler, M. Toner, *Ann. N. Y. Acad. Sci.* **2005**, *1066*, 119.
[10] M. Verheijen, M. Lienhard, Y. Schrooders, O. Clayton, R. Nudischer, S. Boerno, B. Timmermann, N. Selevsek, R. Schlapbach, H. Gmuender, S. Gotta, J. Geraedts, R. Herwig, J. Kleinjans, F. Caiment, *Sci. Rep.* **2019**, *9*, 4641.
[11] A. L. DeVries, D. E. Wohlschlag, *Science* **1969**, *163*, 1073.
[12] A. L. Devries, Y. Lin, *Biochim. Biophys. Acta, Protein Struct.* **1977**, *495*, 388.
[13] Z. Jia, C. I. DeLuca, H. Chao, P. L. Davies, *Nature* **1996**, *384*, 285.
[14] L. Chen, A. L. DeVries, C.-H. Cheng, *Proc. Natl. Acad. Sci. U. S. A.* **1997**, *94*, 3811.
[15] C. I. Biggs, T. L. Bailey, G. Ben, C. Stubbs, A. Fayter, M. I. Gibson, *Nat. Commun.* **2017**, *8*, 1546.
[16] M. I. Gibson, C. A. Barker, S. G. Spain, L. Albertin, N. R. Cameron, *Biomacromolecules* **2009**, *10*, 328.
[17] F. Bachtiger, T. R. Congdon, C. Stubbs, M. I. Gibson, G. C. Sosso, *Nat. Commun.* **2021**, *12*, 1323.
[18] C. I. Biggs, C. Stubbs, B. Graham, A. E. Fayter, M. Hasan, M. I. Gibson, *Macromol. Biosci.* **2019**, *19*, 1900082.
[19] B. L. Wilkinson, R. S. Stone, C. J. Capicciotti, M. T. Andersen, M. I. Matthews, N. H. Paxker, R. B. Ben, R. J. Payne, *Angew. Chem., Int. Ed.* **2012**, *51*, 3606.
[20] Y. D. Kim, W. H. Jung, D. J. Ahn, D. K. Lim, *Nano Lett.* **2023**, *23*, 9500.
[21] H. Geng, X. Liu, G. Shi, G. Bai, J. Ma, J. Chen, Z. Wu, Y. Song, H. Fang, J. Wang, *Angew. Chem., Int. Ed.* **2017**, *129*, 1017.

[22] G. Bai, D. Gao, Z. Liu, X. Zhou, J. Wang, *Nature* **2019**, *576*, 437.
[23] G. Bai, Z. Song, H. Geng, D. Gao, K. Liu, S. Wu, W. Rao, L. Guo, J. Wang, *Adv. Mater.* **2017**, *29*, 1606843.
[24] J. Lee, S. Y. Lee, D.-K. Lim, D. J. Ahn, S. Lee, *J. Am. Chem. Soc.* **2019**, *141*, 18682.
[25] N. Jeon, I.-h. Jeong, E. Cho, I. Choi, J. Lee, E. H. Han, H. J. Lee, P. C. W. Lee, E. Lee, *JACS Au* **2023**, *3*, 154.
[26] C. Lee, Y. Lee, W. H. Jung, T.-Y. Kim, T. Kim, D.-N. Kim, D. J. Ahn, *Sci. Adv.* **2022**, *8*, eadd0185.
[27] T. K. Won, B. Y. Jung, D. J. Ahn, *Nano Lett.* **2024**, *24*, 13662.
[28] K. A. Murray, M. I. Gibson, *Nat. Rev. Chem.* **2022**, *6*, 579.
[29] M. Calderon, M. A. Quadir, S. K. Sharma, R. Haag, *Adv. Mater.* **2010**, *22*, 190.
[30] P. Pouyan, M. Cherri, R. Haag, *Polymers* **2022**, *14*, 2684.
[31] D. Wilms, S.-E. Stiriba, H. Frey, *Acc. Chem. Res.* **2009**, *43*, 129.
[32] S. E. Kim, Y.-R. Lee, M. Kim, E. Seo, H.-J. Paik, J. C. Kim, J.-E. Jeong, Y. I. Park, B.-S. Kim, S.-H. Lee, *Polym. Chem.* **2022**, *13*, 1243.
[33] J. Kim, S. Choi, J. Back, Y. I. Park, J. C. Kim, J.-E. Jeong, H. Jung, T.-H. Kwon, B.-S. Kim, S.-H. Lee, *Adv. Funct. Mater.* **2023**, *33*, 2302086.
[34] S. Y. Lee, M. Kim, T. K. Won, S. H. Back, Y. Hong, B.-S. Kim, D. J. Ahn, *Nat. Commun.* **2022**, *13*, 6532.
[35] C. Yu, L. Ma, K. Li, S. Li, Y. Liu, Y. Zhou, D. Yan, *Phys. Chem. Chem. Phys.* **2016**, *18*, 22446.
[36] S. Wu, Z. He, J. Zang, S. Jin, Z. Wang, J. Wang, Y. Yao, J. Wang, *Sci. Adv.* **2019**, *5*, eaat9825.
[37] P. McConville, J. M. Pope, *Polymer* **2001**, *42*, 3559.
[38] T. Visser, J. H. Mass, *J. Raman Spectrosc.* **1977**, *6*, 114.
[39] A. V. Cresce, S. M. Russell, O. Borodin, J. A. Allen, M. A. Schroeder, M. Dai, J. Peng, M. P. Gobet, S. G. Greenbaum, R. E. Rogers, K. Xu, *Phys. Chem. Chem. Phys.* **2017**, *19*, 574.
[40] C. Vega, M. M. Conde, A. Patrykiejew, *Mol. Phys.* **2006**, *104*, 3583.
[41] A. B. Sultani, L. A. M. Curtis, J. A. Elliott, L. E. McGann, *Sci. Rep.* **2016**, *6*, 34393.
[42] K. L. D. Skinner, G. H. Henry, C. Cataisson, T. Tabib, J. C. Gwilliam, N. J. Watson, E. M. Bullwinkle, L. Falkenburg, R. C. O'Neill, A. Morin, J. S. Wiest, *J. Vis. Exp.* **2014**, *91*, e51312.
[43] J. Wang, M. Satoh, *Langmuir* **2020**, *26*, 13607.